Icarus 211 (2011) 389–400

Contents lists available at ScienceDirect

Icarus

journal homepage: www.elsevier.com/locate/icarus

Magnitude of global contraction on Mars from analysis of surface faults: Implications for martian thermal history

Amanda L. Nahm [a,b,c,*], Richard A. Schultz [a]

[a] Geomechanics – Rock Fracture Group, Department of Geological Sciences and Engineering, MS 172, University of Nevada, Reno, NV 89557-0138, United States
[b] Center for Lunar Science and Exploration, USRA – Lunar and Planetary Institute, 3600 Bay Area Blvd., Houston, TX 77058, United States
[c] NASA Lunar Science Institute, United States

ARTICLE INFO

Article history:
Received 27 March 2010
Revised 1 November 2010
Accepted 2 November 2010
Available online 11 November 2010

Keywords:
Tectonics
Thermal histories
Mars, Surface

ABSTRACT

Faults provide a record of a planet's crustal stress state and interior dynamics, including volumetric changes related to long-term cooling. Previous work has suggested that Mars experienced a pulse of large-scale global contraction during Hesperian time. Here we evaluate the evidence for martian global contraction using a recent compilation of thrust faults. Fault-related strains were calculated for wrinkle ridges and lobate scarps to provide lower and upper bounds, respectively, on the magnitude of global contraction from contractional structures observed on the surface of Mars. During the hypothesized pulse of global contraction, contractional strain of −0.007% to −0.13% is indicated by the structures, corresponding to decreases in planetary radius of 112 m to 2.24 km, respectively. By contrast, consideration of all recognized thrust faults regardless of age produces a globally averaged contractional strain of −0.011% to −0.22%, corresponding to a radius decrease of 188 m to 3.77 km since the Early Noachian. The amount of global contraction predicted by thermal models is larger than what is recorded by the faults at the surface, paralleling similar studies for Mercury and the Moon, which suggests that observations of fault populations at the surface may provide tighter bounds on planetary thermal evolution than models alone.

1. Introduction

The surface record of tectonic deformation provides a record of a planet's thermal and tectonic evolution (Solomon and Chaiken, 1976; Banerdt et al., 1992; Schubert et al., 1992; Watters, 1993; Andrews-Hanna et al., 2008; Zuber et al., 2010). This relationship has been used on Mercury, the Moon, Mars, and icy outer planet satellites in an attempt to understand and bound the thermal evolution of these bodies. Cooling of a planet's interior would create a net global contraction, which would induce global compressional horizontal stress and contractional strain near the surface (Solomon and Chaiken, 1976; Turcotte, 1983; Solomon, 1986; Banerdt et al., 1992; Schubert et al., 1992; Hauck et al., 2004), potentially resulting in the formation of contractional structures at the surface, such as thrust faults (expressed as either wrinkle ridges or lobate scarps). Wrinkle ridges consist of narrow, asymmetric ridges superimposed on broad arches (Plescia and Golombek, 1986; Banerdt et al., 1992; Watters, 1993) and are interpreted to be anticlines above blind thrust faults (Schultz, 2000; Okubo and Schultz, 2004; Tanaka et al., 2010). They are observed on all terrestrial bodies, including Mercury, Venus, the Moon, and Mars (e.g., Watters 1988). On Mars, wrinkle ridges are distributed globally and occur primarily in Hesperian ridged plains (Hr) (Tanaka et al., 1991; Banerdt et al., 1992; Watters, 1993; Mangold et al., 2000; Head et al., 2002). Lobate scarps are interpreted to be the result of surface-breaking thrust faults (Howard and Muehlberger, 1973; Strom et al., 1975; Lucchitta, 1976; Cordell and Strom, 1977; Binder, 1982; Binder and Gunga, 1985; Watters, 1993; Schultz, 2000; Hauck et al., 2004) and are found on Mercury, Mars, and the Moon. On Mars, the majority of lobate scarps occurs in older geologic terranes (in units Npl_1, Npl_2, Npl_d) and they appear to be primarily Noachian in age (Scott and Tanaka, 1986; Greeley and Guest, 1987; Tanaka et al., 1991; Watters, 1993; Mangold et al., 2000).

Theoretical considerations from thermal evolution models and observations, such as the abundance of lobate scarps on the surface, suggest that Mercury has undergone global contraction (e.g., Strom et al., 1975; Watters et al., 1998; Watters and Nimmo, 2010), with a minimum estimate of planetary radius decrease of 0.8 km (Watters et al., 2009) and a maximum estimate of 17 km, resulting from the complete solidification of an initially molten core (Solomon 1976). Similarly, models for the thermal evolution of the Moon have been evaluated by using tectonic structures on the surface (Golombek and McGill, 1983; Turcotte, 1983; Solomon,

* Corresponding author at: Center for Lunar Science and Exploration, USRA – Lunar and Planetary Institute, 3600 Bay Area Blvd., Houston, TX 77058, United States. Fax: +1 281 486 2162.
E-mail address: nahm@lpi.usra.edu (A.L. Nahm).

0019-1035/$ - see front matter © 2010 Elsevier Inc. All rights reserved.
doi:10.1016/j.icarus.2010.11.003

1986). These studies conclude that there has been little or no decrease in lunar radius (<1 km) since the end of the heavy bombardment and emplacement of the maria 3.8 byr ago (Solomon and Chaiken, 1976; Cordell and Strom, 1977; Solomon, 1986; Solomon and Head, 1979, 1980; Golombek and McGill, 1983; Watters and Johnson, 2010). Recent work (Watters et al., 2010) has identified a number of apparently young (<1 Ga) lobate scarps in the lunar highlands. They suggest that the small-scale lobate scarps accommodate late-stage global contraction corresponding to a planetary radius decrease of ~100 m. The identification of these and potentially other lobate scarps in the newly acquired imagery may place additional constraints on thermal evolution models of the Moon.

Net global expansion is an important process for the outer planet satellites. On icy satellites, ice phase transitions in the interior may lead to satellite expansion. The phase change from liquid water to ice I produces large tensile surface stresses (Cassen et al., 1979; Squyres and Croft, 1986; Nimmo, 2004; Collins et al., 2010) and extensional structures at the surface. The transition from ice V to ice II may lead to an increase in surface area of 1% (Squyres and Croft, 1986). Expansion as a result of this process may lead to surface area increases of up to several percent given complete freezing of small satellites (Squyres and Croft, 1986). Satellite differentiation by movement of silicate material to the core and less dense ice to the surface leads to a decrease in mean satellite density, requiring an increase in volume (Squyres and Croft, 1986). On Ganymede and Callisto, the total increase in surface area could be as much as 6% (Squyres, 1980; Squyres and Croft, 1986), and radius increases have been inferred (Squyres, 1980; Mueller and McKinnon, 1988; Collins et al., 2010) to have occurred as a result.

Thermal history models for Mars suggest that the planet was initially hot and subsequently cooled over geologic time (Schubert and Spohn, 1990; Schubert et al., 1992). These models predict a long period of global contraction as a result of the cooling of the interior, although the rate of contraction was not necessarily constant; a global array of contractional structures (wrinkle ridges and lobate scarps) is cited as evidence of this global contraction (Schubert and Spohn, 1990; Tanaka et al., 1991; Zimbelman et al., 1991; Schubert et al., 1992; Watters, 1993; Golombek and Phillips, 2010).

The hypothesis that Mars underwent a period, or pulse, of enhanced global contraction during the Late Noachian (LN) through the Early Hesperian (EH) was first made by Schubert et al. (1992) as a likely explanation for the abundance of wrinkle ridges in Hesperian-aged rocks (e.g., Tanaka et al., 1991). The Early Hesperian basaltic plains units correspond to a global-scale volcanic resurfacing event (Tanaka et al., 1988; Greeley and Schneid, 1991; Frey, 1992; Watters, 1993; Head et al., 2002). Since then, many studies (e.g. Watters, 1993; Mangold et al., 2000; Andrews-Hanna et al., 2008; Golombek and Phillips, 2010) have assumed a causal relationship between contractional structures on Mars and global contraction, yet the correspondence between the two has remained only qualitative.

Several previous studies of tectonic and loading models of Tharsis have invoked stresses related to global thermal contraction to fit the location of the suite of wrinkle ridges surrounding Tharsis (Tanaka et al., 1991; Watters, 1993; Dimitrova et al., 2008), the formation of lobate scarps along the eastern dichotomy boundary (Watters, 2003a,b), and concentric thrust faults around Utopia Basin (Searls and Phillips, 2007). Although a few studies have been conducted on the amount of global contractional strain that should be predicted from thermal models (Hauck et al., 2003; Andrews-Hanna et al., 2008), to date the amount of global contractional strain accommodated at the surface of Mars by thrust faults has not been quantified, hindering a quantitative test of global contraction predictions.

The global contraction of Mars is hypothesized to have peaked during the Late Noachian to Early Hesperian (3.8–3.6 Ga; Hartmann and Neukum, 2001) based on the abundance of wrinkle ridges found in rocks of this age (e.g., Tanaka et al., 1991; Watters, 1993). However, thermal evolution models (Schubert and Spohn, 1990; Schubert et al., 1992; Andrews-Hanna et al., 2008) imply that secular cooling of Mars' interior began in the Early Noachian and continued through the present, predicting an increasing accumulation of compressional stress and contractional strain at the surface. These models also imply that if the compression was global in extent as has been hypothesized, all units older than Early Hesperian should contain contractional structures such as wrinkle ridges.

The hypothesis that the wrinkle ridges and lobate scarps were formed in association with global contraction on Mars is tested here by calculating the horizontal crustal strain accommodated by the contractional structures for two time periods. First, we test the hypothesis of a pulse of global contraction during the Late Noachian through the Early Hesperian. Then we test the cumulative magnitude of global contraction from the Early Noachian through the Late Amazonian. Strain for both scenarios is converted into planetary radius change, permitting a quantitative comparison between fault-related strain and strain predicted by models of the thermal evolution of Mars. We then discuss the implications of our findings for the magnitudes of global contraction predicted for Mars and for Mercury.

2. The global contraction hypothesis

Following the Mariner 9 mission in 1971, the view of Mars was that its surface was dominated by extensional structures, such as normal faults and graben (Schubert et al., 1992). Thermal history models based on these early observations involved net global warming and required planetary expansion over much of Mars' history (Solomon and Chaiken, 1976; Schubert et al., 1992), consistent with the extensive graben systems in Tharsis (Hartmann, 1973; Carr, 1974; Solomon and Chaiken, 1976; Schubert et al., 1992) and elsewhere.

Following the imaging of numerous contractional structures by Viking Orbiter, the view of martian geologic and thermal histories changed significantly. The abundance of globally distributed contractional structures has been cited as evidence for planetary contraction associated with net cooling of the martian interior (Schubert and Spohn, 1990; Tanaka et al. 1991; Zimbelman et al., 1991; Schubert et al., 1992; Watters, 1993; Golombek and Phillips, 2010). During planetary cooling predicted by the thermal models (Schubert and Spohn, 1990; Schubert et al., 1992), the magnitude of horizontal compressional stress at the surface would initially increase in the Early Noachian, then decrease to a minimum at the present time. This appears to be in qualitative agreement with the temporal distribution of contractional structures, with a large number inferred to have been formed in the Late Noachian to Early Hesperian (Scott and Tanaka, 1986; Greeley and Guest, 1987; Tanaka et al., 1991; Watters, 1993). Thermal history models additionally predict monotonically declining volcanism (Schubert and Spohn, 1990; Schubert et al., 1992), in contrast with an apparent pulse in the total area and average rate of volcanism in the Early Hesperian (Zimbelman et al., 1991; Frey, 1992; Watters, 1993).

Hauck et al. (2003) calculated the surface horizontal contractional strain for several scenarios. For global thermal contraction due to planetary heat loss and core growth, they calculate strain rates on the order of $10^{-20}\ s^{-1}$ in the Hesperian, corresponding to an average value of ~0.003% contractional strain (Hauck et al., 2003). For contraction due to extensive Hesperian volcanism (Tanaka et al., 1988; Greeley and Schneid, 1991; Frey, 1992; Watters, 1993; Head et al., 2002), they calculate ~0.0005% surface contractional strain (Hauck et al., 2003). More recently, Andrews-Hanna et al. (2008) used the thermal evolution model

of Hauck and Phillips (2002) to calculate the magnitude of accumulated global contractional strain for several contributing factors. For thermal contractional strain from planetary cooling alone, they calculate ~0.015% strain for the Late Noachian–Early Hesperian (LN–EH). Contractional strain from olivine–spinel phase changes in the mantle is calculated to be ~0.0022% and for the volume reduction from volcanic eruptions from Tharsis the contractional strain is ~0.016% for the same time period. They find the total contractional strain from all sources considered for the Late Noachian–Early Hesperian to be ~0.033%, which is approximately 11 times larger than the estimate by Hauck et al. (2003). The difference between these estimates is likely due to the combination of differing timescales used in each study (100 Myr [Hauck et al., 2003] vs. 250 Myr [Andrews-Hanna et al., 2008]) and the inclusion of more sources of strain in the Andrews-Hanna et al. (2008) model.

The distribution of wrinkle ridges across Mars is uneven, with the structures being confined primarily to volcanic ridged plains units of Early Hesperian age, suggesting that ridge formation may have occurred preferentially during that time (Watters and Maxwell, 1983, 1986; Schubert et al., 1992; Watters, 1993; Mangold et al., 2000). The largest concentration of wrinkle ridges is located in the ridged plains surrounding Tharsis in the western hemisphere, where the structures are oriented approximately circumferentially to the center of the load (Wise et al., 1979; Watters and Maxwell, 1986) (Fig. 1). Secondary concentrations of wrinkle ridges and lobate scarps in the western hemisphere are not circumferential to Tharsis and include Memnonia and Noachis Terra (Watters, 1993) (Fig. 1). In the eastern hemisphere, contractional structures do not exhibit hemisphere-scale patterns, but instead show local- and regional-scale trends (Watters, 1993). The largest concentrations of contractional structures in the eastern hemisphere occur in Hesperia Planum, Terra Cimmeria, Syrtis Major, Arabia Terra, Elysium Planitia (Watters, 1993), and the Utopia and Isidis basins (Golombek and Phillips, 2010) (Fig. 1). However, global contraction has been suggested to be a necessary contributor to the formation of contractional structures everywhere on the planet (e.g., Golombek and Phillips, 2010) but not to fault orientation, which is controlled by regional or local stresses as well as crustal thickness variations (Beuthe, 2010).

3. Evaluation of global contraction

3.1. Strain and radius change predicted by thermal models

Quantitative predictions of surface contractional strain as a function of time are available from Andrews-Hanna et al. (2008) using the thermal evolution model of Hauck and Phillips (2002). Andrews-Hanna et al. (2008) calculate the magnitude of accumulated global contractional stress and strain inferred from the locations of strike-slip faults near Tharsis. They use both the compositional model of Lodders and Fegley (1997) (hereafter referred to as L&F) for Mars enriched in ^{40}K and a chondritic radionuclide abundance following the compositional model of Wänke and Dreibus (1994) (hereafter referred to as W&D) in the thermal evolution model of Hauck and Phillips (2002) to calculate the accumulated contractional strain through time. Both thermal models begin at 4.5 Ga, shortly after differentiation of the planet and magma-ocean overturn would be expected to be complete (Lee and Halliday, 1997; Elkins-Tanton et al., 2005; Andrews-Hanna et al., 2008) and an initially thin lithosphere would have begun to form (Andrews-Hanna et al., 2008). For the W&D model, there is an increase in the thermal contractional strain at the planetary surface up to ~0.227% due solely to planetary cooling after 4.5 Gyr (i.e., to the present time), while the L&F model predicts early heating (from 4.28 to 4.5 Ga) and volumetric expansion due to the heat flux from ^{40}K decay (Andrews-Hanna et al., 2008). Andrews-Hanna et al. (2008) use the convention that contractional strain is positive, so the planetary expansion predicted during this time by the L&F model is shown as negative values in Fig. 2. After the early period of expansion, the contractional strain history of the L&F model is similar to the W&D model, with a cumulative contractional strain from planetary cooling at the surface of ~0.236% after 4.5 Gyr (Andrews-Hanna et al., 2008) (Fig. 2).

In addition to thermal contraction from the cooling of the planet, olivine–spinel phase changes within the mantle lead to further contraction (Andrews-Hanna et al., 2008). The phase change contractional strain of 0.016% is in addition to that due to cooling of the mantle (Andrews-Hanna et al., 2008). Another likely source of contraction is plume-induced volcanic activity during the formation of Tharsis (Tanaka et al., 1991; Andrews-Hanna et al., 2008), since the rise of mantle plumes would have removed a large volume of partial melt from the mantle while transferring a substantial amount of heat to the surface (Andrews-Hanna et al., 2008). This component results in additional contractional strain of 0.06% due to the formation of Tharsis between 4.5 and 3.7 Ga (Andrews-Hanna et al., 2008).

The total contractional strain predicted by the thermal evolution models as a function of time, including all three components discussed above, is shown in Fig. 2, with the grey dotted line being the L&F compositional model and the black solid line representing the W&D compositional model. The strain accumulated at the surface during the time of the hypothesized Hesperian pulse of global

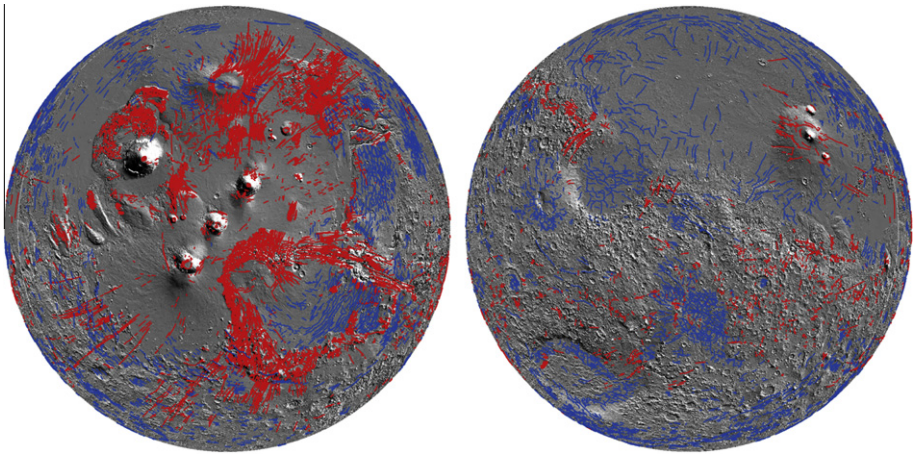

Fig. 1. Global distribution of faults on Mars; data from Knapmeyer et al. (2008). Red: extensional faults, Blue: contractional faults. Western hemisphere, left and eastern hemisphere, right.

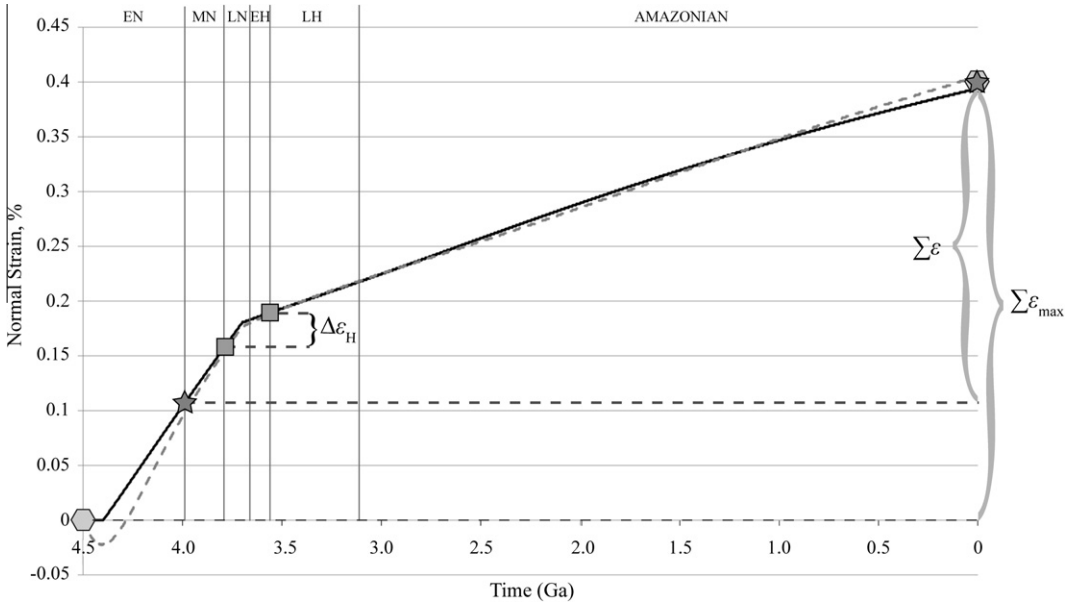

Fig. 2. Total predicted contractional strain, in percent, as a function of time, from thermal history models (after Andrews-Hanna et al. (2008)). EN: Early Noachian, LN: Late Noachian, EH: Early Hesperian, LH: Late Hesperian (dates from Hartmann and Neukum (2001)). Contractional strain is positive, extensional strain is negative; Black solid line: W&D model; Grey dashed line: L&F model; $\Delta\varepsilon_H$: amount of contractional strain accumulated during the hypothesized pulse of global contraction (LN–EH); $\sum\varepsilon$: amount of contractional strain accumulated since the age of the oldest thrust faults; $\sum\varepsilon_{max}$: total amount of contractional strain predicted by thermal models.

contraction is $\Delta\varepsilon_H = 0.033\%$ (Fig. 2), which is the same for either compositional model. The total amount of contractional strain accumulated since the Early Noachian (EN), the age of the earliest thrust faults identified on Mars' surface (Knapmeyer et al. 2008), is shown by $\sum\varepsilon = \sim 0.3\%$ (Fig. 2). An upper limit on the value of predicted cumulative contractional strain ($\sum\varepsilon_{max}$) i.e., from the Early Noachian to the Late Amazonian, is ~0.4% for both models, obtained by including the earliest period of martian history that predates the recognized surface geology.

3.2. Contractional strain from structures

3.2.1. Fault database

The recent comprehensive database of faults obtained by Knapmeyer et al. (2006, 2008) was used in this study. These normal and thrust faults were mapped for their database on 1 km/pixel Mars Orbiter Laser Altimeter (MOLA) digital elevation models and were assigned maximum ages based on crater retention ages of the global 1:15,000,000 scale geologic maps of Mars (Scott and Tanaka, 1986; Scott et al., 1987a, b; Knapmeyer et al., 2006, 2008). Nearly 15,000 faults have been mapped globally (Knapmeyer et al., 2008) in all ages of rocks (Fig. 1). More than half of these structures are normal faults, ranging in length from ~600 m to more than 1400 km (Knapmeyer et al., 2008). The remainder of these structures is classified as thrust faults, which range in length from ~7 km to approximately 650 km (Knapmeyer et al., 2008). Knapmeyer et al. (2006, 2008) did not distinguish between lobate scarps and wrinkle ridges in their dataset.

The Knapmeyer et al. (2006, 2008) database is divided into normal faults ($N = 9675$) and thrust faults ($N = 5142$) ranging in age from Early Noachian to Late Amazonian. Of the faults mapped by Knapmeyer et al. (2006, 2008), 6% of normal faults and 1.8% of thrust faults are classified as Early Noachian in age (3.99–3.95 Ga; Hartmann and Neukum, 2001), 41.8% of normal faults and 21.9% of thrust faults are classified as Middle Noachian (3.95–3.8 Ga), 22.8% of normal faults and 48.4% of thrust faults are classified as Late Noachian (3.8–3.7 Ga), 4.8% of normal faults and 13.2% of thrust faults are classified as Early Hesperian (3.7–3.6 Ga), 11.4% of normal faults and 10.3% of thrust faults are classified as Late Hesperian (3.6–3.15 Ga), 9.8% of normal faults and 1.8% of thrust faults are classified as Amazonian (3.15–0 Ga), and the remaining 3.4% and 2.5%, respectively, were not assigned an age and consequently were not used in this study.

3.2.2. Strain and radius change calculated from structures

To quantitatively test the hypothesis that Mars underwent a period of global contraction, the fault-related strains and corresponding radius changes must be calculated. For this study, the Knapmeyer et al. (2006, 2008) fault database was divided into two time periods: Early Noachian to Late Amazonian (0–3.99 Ga; Hartmann and Neukum, 2001), corresponding to the cumulative global cooling-related strain and Late Noachian to Early Hesperian (3.6–3.8 Ga), corresponding to the Early Hesperian pulse. Fault lengths of both normal and thrust faults were considered for these two time intervals.

The calculations carried out in this study are divided into several cases (Tables 1 and 2), with a range of plausible fault scaling relationships (described below). Case 1 tests the hypothesis of a pulse of global contraction during the Late Noachian–Early Hesperian (LN–EH). Case 1a considered all thrust faults in the Knapmeyer et al. (2008) database to be wrinkle ridges, providing a lower bound to the contractional strain and planetary radius decrease accommodated by the contractional structures, while case 1b considers all thrust faults to be lobate scarps, thus providing an upper bound on the contractional strain and planetary radius decrease for this time period. Case 2 tests the total predicted global contraction against the complete geologic record of contractional structures. Case 2a also considered all thrust faults in the Knapmeyer et al. (2008) database to be wrinkle ridges, providing a lower bound to the contractional strain and planetary radius decrease during Early Noachian–Late Amazonian time. Case 2b considers the thrust faults to be lobate scarps, providing an upper bound to values of strain and radius decrease calculated for this time interval. Thus, the horizontal normal strains and corresponding radius decreases were calculated for thrust faults as wrinkle ridges and as lobate scarps for the LN–EH and EN–LA (Tables 1 and 2).

Table 1
Results of the strain and radius change calculations, calculated with γ_{avg} for lobate scarps: 2.5×10^{-3}, γ_{avg} for normal faults: 5×10^{-4}, and γ_{avg} for wrinkle ridges: 2.5×10^{-4}. Negative values, contractional strain and radius decrease; positive values, extensional strain and radius increase. EN: Early Noachian; LN: Late Noachian; EH: Early Hesperian; LA: Late Amazonian; ε_n: horizontal normal strain. WR: wrinkle ridges; LS: lobate scarps; NF: normal faults.

Case	Time interval	Structure type	% Strain (ε_n)	Radius change (km)	Net radius change (km)
1a	LN–EH	WR	−0.007	−0.112	0.68
		NF	0.046	0.787	
1b		LS	−0.066	−1.12	−0.33
		NF	0.046	0.787	
2a	EN–LA	WR	−0.011	−0.188	1.49
		NF	0.099	1.68	
2b		LS	−0.111	−1.89	−0.21
		NF	0.099	1.68	

Table 2
Results of the strain and radius change calculations, calculated with γ_{avg} for lobate scarps: 5×10^{-3}, γ_{avg} for normal faults: 5×10^{-3}, and γ_{avg} for wrinkle ridges: 5×10^{-4}. Negative values, contractional strain and radius decrease; positive values, extensional strain and radius increase. EN: Early Noachian; LN: Late Noachian; EH: Early Hesperian; LA: Late Amazonian; ε_n: horizontal normal strain. WR: wrinkle ridges; LS: lobate scarps; NF: normal faults.

Case	Time interval	Structure type	% Strain (ε_n)	Radius change (km)	Net radius change (km)
1a	LN–EH	WR	−0.013	−0.22	7.62
		NF	0.463	7.85	
1b		LS	−0.132	−2.24	5.61
		NF	0.463	7.85	
2a	EN–LA	WR	−0.022	−0.38	16.34
		NF	0.987	16.72	
2b		LS	−0.222	−3.77	12.95
		NF	0.987	16.72	

Horizontal normal strain and planetary radius increases due to normal faulting were also calculated for both the LN–EH and EN–LA periods (Tables 1 and 2). Since the net radius change may be more representative of the total global fault-related strains, as has been shown for both the Moon (e.g. Golombek and McGill, 1983) and for icy outer planet satellites (e.g., Squyres, 1980; Mueller and McKinnon, 1988; Collins et al., 2010), values for the net radius change for Mars were calculated by subtracting the radius decrease (from contraction) from the radius increase (from extension).

Unlike the icy satellites, the stresses that formed the extensional structures (normal faults and graben) on Mars likely did not result from a global expansion event, but rather from regional or local sources. As many extensional structures are present on and around Tharsis and Alba Patera (Fig. 1), it is likely that their formation is related to a variety of volcanomagmatic processes (e.g., Banerdt et al., 1992; Mège and Masson, 1996; McGovern et al., 1999, 2001; Scott et al., 2002; Hauber and Kronberg, 2001, 2005; Wilson and Head, 2002; Cailleau et al., 2003; Ivanov and Head, 2006; Hauber et al., 2010). The large values of apparent global expansion we obtain in this paper attest instead to the importance of local and regional sources of extensional strains.

The surface strain and corresponding planetary radius change associated with faults scale with the maximum fault offset or displacement (D_{max}). We calculate horizontal normal strain (i.e., fault-normal extension or contraction, or heave) and radius change using displacement–length (D_{max}/L) scaling, in parallel to what has been done in previous studies for Mercury (e.g. Watters et al., 1998, 2009) and the Moon (e.g., Watters and Nimmo, 2010) by using standard methods (e.g., Scholz and Cowie, 1990; Scholz, 1997; Schultz et al., 2010). Representative D_{max}/L ratios (γ) for normal faults, surface-breaking thrust faults (lobate scarps), and wrinkle ridges were used to calculate the total horizontal normal strain for each set of fault ages (LN–EH and EN–LA).

When compared to typical terrestrial D_{max}/L values, less displacement per unit length is accommodated along martian faults (Schultz et al., 2006), resulting in lower D/L ratios. For example, martian D_{max}/L ratios for thrust faults range between $\sim 2 \times 10^{-3}$ and 7.5×10^{-3} (Schultz et al., 2006), where typical values of γ for terrestrial thrust faults are between $\sim 5 \times 10^{-3}$ and $\sim 5 \times 10^{-2}$ (Bergen and Shaw, 2010). For martian normal faults, γ ranges between $\sim 1 \times 10^{-2}$ and 3×10^{-3} (Schultz et al., 2006; Polit et al., 2009); γ for terrestrial normal faults ranges from $\sim 2 \times 10^{-2}$ to $\sim 5 \times 10^{-2}$ (Bergen and Shaw, 2010). Based on the values listed above, we adopt D_{max}/L values of 5×10^{-3} and 1×10^{-2} for surface-breaking thrust faults and 1×10^{-3} and 1×10^{-2} for normal faults to bound values of calculated strain and corresponding radius change.

Mechanical modeling shows that a reduction in fault displacement by an order of magnitude reduces the amplitude of the anticline that forms above the fault tip by a comparable amount, thereby supporting the reduction of the D/L ratio by an order of magnitude for wrinkle ridges. Interestingly, wrinkle ridges in much of the Tharsis region lack wrinkles (Okubo and Schultz, 2004), indicating that flexural slip folding was not important for these structures. Instead, smaller anticline amplitudes must be related to reduced fault displacements relative to lobate thrust-fault scarps, probably due to material differences or stress magnitudes between wrinkle ridges and lobate scarp terranes. Therefore, values for the D_{max}/L ratio for wrinkle ridges in this study are taken to be those for lobate scarps reduced by one order of magnitude, i.e., 5×10^{-4} and 1×10^{-3}.

The magnitude of radius change based on these calculations is sensitive to lithospheric thickness or faulting depth T, which has

been inferred to have increased through time as Mars cooled, to a maximum lithospheric thickness of ~100 km presently in Syria Planum (Zuber et al., 2000). For example, Beuthe (2010) showed that lithospheric thickness at the time of contraction (or expansion) has an effect on the deformation. He showed that east–west striking thrust faults are predicted to form preferentially where the lithosphere was modeled to be thinnest. Additionally, strain magnitude and radius change are related to the depth of faulting T. As T increases, the magnitude of the radius change decreases for all fault types. However, given that the majority of faults used in this study (>90%) formed between the Early Noachian and Late Hesperian, values for faulting depth determined from forward mechanical modeling of structural topography of individual faults (see Schultz et al. (2010) for a review) that formed during this time are assumed to be representative values for the faults in the catalog. Therefore, strain and corresponding radius change values were calculated for faulting depths T of 30 km for lobate scarps (Schultz and Watters, 2001; Grott et al., 2007), 30 km for wrinkle ridges (Okubo and Schultz, 2004), and 15 km for normal faults (Wilkins et al., 2002; Polit et al., 2009) as determined by inversion of fault-related topography.

Brittle strain is the inelastic deformation produced by tectonic activity at the surface. The average brittle strain in a region is determined by summing the deformation accommodated by all faults in the region during any given time interval (Scholz, 1997). For a volume V containing a population of faults, the resultant brittle horizontal normal strain ε_n is given by Kostrov's relation (see Scholz, 1997; Schultz et al., 2010),

$$\varepsilon_n = \frac{\sin\delta\cos\delta}{V}\sum_{i=1}^{N} D_i L_i H_i \tag{1}$$

where the volume of the deformed region V is defined as

$$V = \frac{4}{3}\pi\left[R_p^3 - (R_p - T)^3\right] \tag{2}$$

and where δ is the fault dip angle ($\delta = 60°$ for normal faults and $\delta = 30°$ for thrust faults beneath lobate scarps and wrinkle ridges), N is the total number of faults in the population, D is the fault displacement (positive for extension, negative for contraction), L is the fault length, H is the down dip fault height, and R_p is the current average radius of Mars (3397 km).

Following Scholz and Cowie (1990), Scholz (1997), Schultz (2003), and Manighetti et al. (2005), the average displacement (D_{avg}) rather than D_{max} is used to calculate fault-related strain. The shape of the fault displacement profile (taken along strike) influences the value of the maximum displacement. Displacement profiles for surface-breaking thrust and normal faults are commonly peaked, where the displacement decreases linearly from D_{max} down to zero displacement at the fault tips (e.g., Dawers et al., 1993; Manighetti et al., 2005), so the average displacement is $D_{avg} = 0.5D_{max}$ (Scholz and Cowie, 1990; Schultz, 2003; Manighetti et al., 2005). This decrease in displacement is incorporated into the strain calculations by using $\gamma_{avg} = 0.5(D_{max}/L)$. Assuming a constant $L/H = 2$ (e.g., Polit et al., 2009) and $\gamma_{avg} = 0.5(D_{max}/L)$, Eq. (1) becomes

$$\varepsilon_{n,avg} = \frac{\gamma_{avg}\sin\delta\cos\delta}{2V}\sum_{i=1}^{N} L_i^3 \tag{3}$$

where values for γ_{avg} for normal faults are 5×10^{-3} and 5×10^{-4}, for thrust faults γ_{avg} values are 5×10^{-3} and 2.5×10^{-3}, and γ_{avg} values for wrinkle ridges are 5×10^{-4} and 2.5×10^{-4}.

In this analysis, we assume that the faults in the catalog are small, or nonrestricted, faults. This assumption is supported by constant (linear) D/L ratios for lobate scarps for Mars and for thrust faults on Earth (Schultz et al., 2006 and references therein). Vertically restricted faults (i.e., faults bounded at depth either by stratigraphy or thermal gradient) show exponential length–frequency distributions, where D decreases as L increases with constant T or H (e.g. Soliva et al., 2005; Polit et al., 2009). Terrestrial earthquake populations define two groups, depending on whether the entire seismogenic thickness is ruptured (large earthquakes) or not (small earthquakes) (Scholz, 1982, 2002). These events are well characterized using nonlinear scaling relationships (Wilkins and Schultz, 2005). The topography of surface-breaking faults is related, in part, to the distribution of earthquake slip at depth (e.g., Cohen, 1999), implying a relationship between fault displacement distribution and seismogenic layer thickness (i.e. the depth to the lower stability transition (LST)). The seismic cycle and the accumulation of fault displacement are not complete without also considering stable creep along the fault at depths greater than the LST between earthquakes (e.g., Tse and Rice, 1986; Marone, 1998). Therefore, although seismicity and coseismic slip may be restricted by the seismogenic thickness, the cumulative fault displacement D may not be, consistent with linear D/L scaling relationships documented for large-scale planetary faults on Earth, Mars, and Mercury. This motivates the use of the nonrestricted, small-fault form of the Kostrov relation (1).

The discrepancy between the small and large-fault solutions for contractional strain can be estimated by comparing the equations for strain due to small and large faults (see Scholz, 1998; Schultz et al., 2010) as

$$\left(\frac{\varepsilon_{small}}{\varepsilon_{large}}\right) = \frac{\left(\frac{\sin\delta\cos\delta}{V}\right)\left(\frac{\gamma_0}{2}\right)\sum_i^N L_i^3}{\left(\frac{\sin\delta\cos\delta}{V}\right)\left(\frac{\gamma_r T}{\sin\delta}\right)\sum_i^N L_i^2} \tag{4}$$

which simplifies to become

$$\left(\frac{\varepsilon_{small}}{\varepsilon_{large}}\right) = \left(\frac{\gamma_0}{\gamma_r}\right)\left(\frac{\sin\delta}{2T}\right)\frac{\sum_i^N L_i^3}{\sum_i^N L_i^2} \tag{5}$$

where ε_{small} is the strain accommodated by small faults, ε_{large} is the strain accommodated for large faults, γ_0 is the D/L ratio for unrestricted faults, and γ_r is the D/L ratio for stratigraphically restricted faults. Using the values for martian lobate thrust-fault scarps and $\gamma_0 = \gamma_r$, (4) equals 0.532. Values of γ_0 and γ_r are available from datasets from Earth (Fumanyá, near Barcelona, Spain; Soliva et al., 2005) and the northern plains of Mars (Polit et al., 2009). For Fumanyá, $\gamma_0/\gamma_r = 0.04/0.011 = 3.64$; for Mars, $\gamma_0/\gamma_r = 0.001/0.0005 = 2.0$. Although γ_r is not a constant, these are its minimum values for these two datasets and they provide an estimate of the maximum difference between the two strain solutions for these cases. Using these values in (5), the ratio of small-fault strain to large-fault strain for the martian lobate scarp dataset is 1.1–1.9, meaning that the large-fault solution to calculate contractional strain and planetary radius decrease is comparable to, or perhaps half of, the actual value that is implied by a constant D/L ratio and the small-fault form of Kostrov's equation. Therefore, the use of the nonrestricted, small-fault form of Kostrov's equation provides a useful upper bound to the horizontal contractional strain that is also consistent with linear D/L scaling of martian lobate scarps.

The values of horizontal normal strain were used to calculate the change in planetary radius using

$$\Delta R = R_p - \sqrt{\frac{R_p^2}{\varepsilon_n + 1}} \tag{6}$$

where ΔR is the change in the martian radius following Watters and Nimmo's (2010) work on the global contraction of Mercury. For contractional faulting, negative values of ε_n yield radius decreases (negative), while positive values of ε_n from extensional faulting yield radius increases (positive).

3.2.3. Results

The results of the horizontal normal strain calculations are listed in Tables 1 and 2. Table 1 shows values calculated using the lower γ_{avg} (lobate scarps: 2.5×10^{-3}, wrinkle ridges: 2.5×10^{-4}, normal faults: 5×10^{-4}), while Table 2 displays the values calculated using the upper γ_{avg} (lobate scarps: 5×10^{-3}, wrinkle ridges: 5×10^{-4}, normal faults: 5×10^{-3}). For the hypothesized pulse of global contraction (LN–EH time interval), the calculated horizontal normal strain for case 1a is −0.007% (assuming all mapped thrust faults are wrinkle ridges) and −0.066% for case 1b (assuming all mapped thrust faults are lobate scarps) (Table 1). Strain for case 2 (i.e., the observed geologic record, EN–LA) was calculated to be −0.011% for the wrinkle ridge case and −0.111% for the lobate scarp case. As shown in Table 2, all values calculated for normal faults using the larger γ_{avg} are 10 times higher than those calculated using the smaller γ_{avg} (Table 1); values calculated for thrust faults (lobate scarps or wrinkle ridges) are two times higher than those shown in Table 1.

These values of strain were converted to values of martian radius change by using Eq. (6), which yields radius decreases of 112 m and 1.12 km for the wrinkle ridge and lobate thrust-fault scarp cases, respectively, during the LN–EH. For the EN–LA, strains reported above correspond to radius decreases of 188 m and 1.89 km for wrinkle ridges and lobate scarps, respectively.

The net radius changes for both cases using two values for γ_{avg} were also calculated. For the normal fault and the wrinkle ridge case for the LN–EH pulse using the lower γ_{avg}, we find a net increase in radius of 675 m; for the normal fault and the lobate scarp case, we find a net decrease of 331 m (Table 1); however, using the upper γ_{avg}, we calculate net radius increases for all cases (Table 2). The net radius increases are calculated to be 7.62 km for wrinkle ridges (1a) and 5.61 km for lobate scarps (1b).

For the EN–LA time interval, we find net radius increases of 1.49 km for the wrinkle ridge case and a decrease of 210 m for the lobate scarp case (Table 1); using the larger γ_{avg}, net radius increases of 16.34 km (2a) and 12.95 km (2b) are calculated (Table 2). These net increases are obtained from extensional structures and converted into a global average increase in planetary radius as has been done for the contractional structures in this study and for Mercury (Strom et al., 1975; Watters et al., 1998; Watters and Nimmo, 2010), and extensional structures on the Moon (Golombek and McGill, 1983) and icy outer planet satellites (Squyres, 1980; Mueller and McKinnon, 1988; Collins et al., 2010), while noting that they likely are associated with local or regional scale uplifts.

Comparison of the calculated fault-related strain with strain predicted by the thermal models (Andrews-Hanna et al., 2008) shows that the thermal models predict substantially more contractional strain than is recorded by the faults in most cases (Tables 3 and 4). Cumulative contractional strains at the martian surface predicted by thermal evolution models exceed those recorded by contractional structures by factors of 4.7–9.7 during the Late Noachian to Early Hesperian pulse and 1.3–27.9 during the Early Noachian to Late Amazonian (Tables 3 and 4). However, for case 1b (normal faults and lobate scarps during the LN–EH), the strain ratios are less than 1, meaning that calculated fault-related strain is larger than what is predicted by the thermal models (Tables 3 and 4). Although this case appears to remedy the discrepancy between the thermal models and fault-related strain, this result again indicates that the thermal models generally over-predict the magnitude of contractional strain and radius change for Mars. This is due to the observation that most thrust faults are manifested at the surface as wrinkle ridges (Tanaka et al., 1991), meaning that case 1b is unlikely to be realistic.

Table 3
Comparison between fault-related strain and strain predicted by the thermal models and corresponding radius change, calculated with γ_{avg} for lobate scarps: 5×10^{-4}, γ_{avg} for normal faults: 2.5×10^{-3}, and γ_{avg} for wrinkle ridges: 2.5×10^{-4}. W&D: Wänke and Dreibus (1994) model; L&F: Lodders and Fegley (1997) model; WR: wrinkle ridges; LS: lobate scarps; LN: Late Noachian; EN: Early Noachian, EH: Early Hesperian; LA; Late Amazonian; Strain ratio: ratio of predicted thermal strain to fault-related strain; strain ratios > 1 mean strain from thermal models > fault-related strain; ΔR: calculated change in radius (Watters and Nimmo, 2010) based on the difference between predicted thermal strain and fault-related strain for both models (W&D and L&F) and lobate scarps and wrinkle ridges; positive values indicate that more strain is predicted by the thermal models than is calculated for the faults.

Case	Time interval	Structure type	Model	Strain ratio	ΔR (km)
1a	LN–EH	WR	W&D	9.32	0.42
		WR	L&F	9.70	0.44
1b		LS	W&D	0.93	−0.59
		LS	L&F	0.97	−0.57
2a	EN–LA	WR	W&D	26.2	4.74
		WR	L&F	27.9	5.06
2b		LS	W&D	2.6	3.05
		LS	L&F	2.8	3.37

Table 4
Comparison between fault-related strain and strain predicted by the thermal models and corresponding radius change, calculated with γ_{avg} for lobate scarps: 5×10^{-3}, γ_{avg} for normal faults: 5×10^{-3}, and γ_{avg} for wrinkle ridges: 5×10^{-4}. W&D: Wänke and Dreibus (1994) model; L&F: Lodders and Fegley (1997) model; WR: wrinkle ridges; LS: lobate scarps; LN: Late Noachian; EN: Early Noachian, EH: Early Hesperian; LA; Late Amazonian; Strain ratio: ratio of predicted thermal strain to fault-related strain; strain ratios > 1 mean strain from thermal models > fault-related strain; ΔR: calculated change in radius (Watters and Nimmo, 2010) based on the difference between predicted thermal strain and fault-related strain for both models (W&D and L&F) and lobate scarps and wrinkle ridges; positive values indicate that more strain is predicted by the thermal models than is calculated for the faults.

Case	Time interval	Structure type	Model	Strain ratio	ΔR (km)
1a	LN–EH	WR	W&D	4.66	0.31
		WR	L&F	4.85	0.33
1b		LS	W&D	0.47	−1.71
		LS	L&F	0.49	−1.68
2a	EN–LA	WR	W&D	13.1	4.55
		WR	L&F	14.0	4.87
2b		LS	W&D	1.3	1.17
		LS	L&F	1.4	1.49

4. Discussion and implications

4.1. Implications for Mars

4.1.1. Hesperian pulse

A decrease in planetary radius of 112 m to 1.12 km is indicated by contractional structures for the Late Noachian–Early Hesperian time (Table 1); using an upper limit of γ_{avg}, decreases of 224 m to 2.24 km are calculated (Table 2). Comparison between the fault-related strain and predicted strain from thermal models shows a discrepancy between these observations and predictions, where the thermal models predict between 4.7 and 9.7 times more contractional strain than is accommodated by wrinkle ridges (Tables 3 and 4).

When the contractional strain magnitude for the pulse is divided by the total cumulative contractional strain for Mars' history, we find that the pulse makes up ~59% of the total contractional strain for Mars. This suggests that a pulse of enhanced contractional deformation occurred during this time, although it may reflect instead that basalt erupted during the Hesperian was preferentially deformed by wrinkle ridges due to regional processes in Tharsis and elsewhere.

The strain rate during the pulse is calculated by using the LN–EH time interval, or 200 Myr, to be between $2.06 \times 10^{-20}\ s^{-1}$ and $2.06 \times 10^{-19}\ s^{-1}$ (Table 5), while the strain rate for this time period predicted by thermal models is $\sim 5.12 \times 10^{-20}\ s^{-1}$, about three times slower (for lobate scarps) and ~3 times faster (for wrinkle ridges) than what was accommodated by the faults. The average slip rate on thrust faults beneath martian wrinkle ridges was thus faster than what would be predicted by models of global cooling alone, supporting additional sources of stress such as Tharsis.

Andrews-Hanna et al. (2008) suggested that wrinkle ridge formation would not have coincided with a peak in the rate of global contraction, as implied by the hypothesis of an Early Hesperian pulse. Instead, formation of wrinkle ridges would have begun once the accumulated contractional stresses were large enough in magnitude to change the faulting regime from predominantly extensional surrounding Tharsis to one that favors thrust faulting (Andrews-Hanna et al., 2008). As global contractional strain accumulated through time, wrinkle ridges would likely have continued to grow (Andrews-Hanna et al., 2008) and new structures may also have formed. Our results suggest that global contraction changed the stress state around Tharsis to predominantly contractional before the end of Noachian time.

4.1.2. Cumulative contraction

We calculated the cumulative contractional strain and corresponding radius decreases for all of Mars' recorded geologic history (Early Noachian to Late Amazonian). A decrease in planetary radius of 188 m to 3.77 km is indicated by contractional structures for this time period (Tables 1 and 2). The values are, again, in most cases, several times smaller than those predicted by thermal models (Tables 3 and 4). Strain rates were also calculated for this time period and range from $8.74 \times 10^{-22}\ s^{-1}$ to $1.76 \times 10^{-20}\ s^{-1}$ (Table 5). The average strain rate for this time period predicted by the thermal models is $\sim 8.11 \times 10^{-21}\ s^{-1}$, ~6 times higher for wrinkle ridges and ~1.6 times slower for lobate scarps than the calculated strain rate. This result may indicate that local and regional sources of stress associated with contractional deformation on Mars waned early in martian history (i.e., by Early Hesperian time), leading to a better correspondence between the long-term average contractional strain magnitude and that predicted by global cooling models.

The existing thermal models for Mars generally over-predict the amount of contractional strain that is accommodated by the contractional structures (except for case 1b, which assumes an observationally unlikely upper limit to fault-related strain; Tables 3 and 4). The discrepancy between strain predicted by the thermal models and the calculated fault-related strain may be evaluated by several possible scenarios. First, the differences between the predicted strain from the thermal models and the calculated fault-related strains were used in Eq. (6) to calculate the amount of radius decrease the planet would have had to have undergone in order for the fault-related strains to match the thermal history predictions. For the LN–EH pulse (wrinkle ridges, case 1a), the thermal models generally predict ~330–440 m more decrease in radius than is accommodated by the observed faults (Tables 3 and 4). For recorded geologic time (EN–LA, case 2), the additional radius decreases required for this period generally range from 1.17 km to 5.06 km (Tables 3 and 4).

Second, during the Early Hesperian, extensive volcanic resurfacing of Mars (>37%) occurred (Tanaka et al., 1988; Greeley and Schneid, 1991; Frey, 1992). It is possible that this resurfacing event covered many Noachian structures that formed as a result of global contraction. Additionally, Amazonian materials overlie older units, covering an additional 1/4 of the surface (Tanaka et al., 1988), which means that approximately 60% of the exposed surface is Early Hesperian or younger. If we assume that the amount of strain from buried thrust faults corresponds to the additional Early Noachian contractional strain predicted by the thermal models ($\sum \varepsilon_{max} - \sum \varepsilon$) of 0.1% (Fig. 2), this results in an additional ~1.7 km of radius decrease. The total amount of radius decrease then would be the sum of the value for the buried thrust faults and the value of the observed fault-related radius decrease, which is 1.89–2.08 km for case 2a (wrinkle ridges) and 3.59–5.47 km for case 2b (lobate scarps). These values are ~1.2–10 times larger than the values of radius decrease during the Early Noachian–Late Amazonian time interval (i.e., 188 m to 3.77 km) (Tables 1 and 2). For the fault-related strain to match the predictions of the thermal models, this extra ~1.7 km would have to be buried in an area ~2/3 the surface area of the planet (based on the approximate surface area of Hesperian and Amazonian age units) (Tanaka et al., 1988; Greeley and Schneid, 1991; Frey, 1992; Watters, 1993; Head et al., 2002).

Given that between 188 and 377 m of contraction are accommodated across the entire planet by the observed wrinkle ridges, faults in the resurfaced 2/3 of Mars would have had to have accommodated up to 9 times more strain than the entire presently exposed surface of Mars. For lobate scarps, 1.89–3.77 km of contraction are accommodated globally. In this scenario, buried faults in the resurfaced portion of Mars would have to have accommodated between 1.5 and 1.9 times more contraction than has been accommodated by lobate scarps presently exposed over the entire planetary surface. In this scenario, the additional contractional strain predicted during the Noachian by the thermal history models is considerably larger than what is recorded in the fault populations. Orders of magnitude greater contractional strains would need to be accommodated by the faults than is observed in order for the models to accurately predict the observations.

Table 5
Calculated strain rates for lobate scarps and wrinkle ridges during time intervals of interest. LN: Late Noachian; EH: Early Hesperian; EN: Early Noachian; LA: Late Amazonian; duration of LN–EH: 200 Myr; duration of EN–LA: 3.99 Gyr; WR: wrinkle ridge; LS: lobate scarp; γ_{avg}: D_{avg}/L used to calculate fault-related strain; values calculated from fault-related strains calculated in this study.

Time interval	Structure type	γ_{avg} value	Strain rate (s^{-1})
LN–EH	WR	2.5×10^{-4}	1.11×10^{-20}
	WR	5×10^{-4}	2.06×10^{-20}
	LS	2.5×10^{-3}	1.05×10^{-19}
	LS	5×10^{-3}	2.06×10^{-19}
EN–LA	WR	2.5×10^{-4}	8.74×10^{-22}
	WR	5×10^{-4}	1.75×10^{-21}
	LS	2.5×10^{-3}	8.74×10^{-21}
	LS	5×10^{-3}	1.76×10^{-20}

4.2. Implications for Mercury

The results of this study have implications for the global tectonics of Mercury, since global contraction from secular cooling has been hypothesized for this planet as well (Cordell and Strom, 1977; Solomon, 1977; Melosh and McKinnon, 1988; Thomas et al., 1988; Watters et al., 1998; Watters et al., 2004; Watters and Nimmo, 2010). A global system of lobate scarps has been observed on Mercury's surface (Murray et al., 1974; Strom et al., 1975; Solomon and Chaiken, 1976; Cordell and Strom, 1977; Melosh and McKinnon, 1988; Thomas et al., 1988; Watters et al., 2009) which suggests that a period of global contraction may have occurred between ~3.5 and 4.0 Ga (Trask and Guest, 1975; Strom et al., 1975; Solomon and Chaiken, 1976; Solomon, 1986; Hauck et al., 2004; Watters et al., 2009; Watters and Nimmo, 2010; Zuber et al., 2010). It has also been suggested that these structures record only a fraction of the total global contraction Mercury has undergone (Watters et al., 2004; Watters et al., 2009; Watters

and Nimmo, 2010). Contractional structures on Mercury far outnumber extensional structures (e.g. Strom et al., 1975; Cordell and Strom, 1977; Watters et al., 2009; Watters and Nimmo, 2010), suggesting that an early planetary compressive stress field may have suppressed the formation of extensional structures at the surface (Cordell and Strom, 1977). Early imagery showed a nearly random azimuthal distribution of lobate scarps suggesting they formed purely by planetary contraction, instead of solely despinning or a combination of the two (Strom et al., 1975; Cordell and Strom, 1977), although newly imaged lobate scarps suggest their distribution is more likely indicative of formation through a combination of global thermal contraction and despinning (Watters and Nimmo, 2010).

Using an average displacement of 1 km for faults dipping between 25° and 45°, Strom et al. (1975) estimated the magnitude of radius decrease accommodated by lobate scarps in the highlands to be 1–2 km. From D/L scaling relationships, Watters et al. (1998) estimate the total contractional strain from the same faults to be 0.043% (for $\theta = 30°$), which corresponds to a radius decrease of 520 m (Watters et al., 2009; Watters and Nimmo, 2010). Images obtained by MESSENGER show lobate scarps not seen in Mariner 10 images and lobate scarps in the originally un-imaged portion of Mercury indicate that the estimates of strain by Strom et al. (1975) and Watters et al. (1998) are too low (Watters et al., 2009; Watters and Nimmo, 2010). Current estimates of global contractional strain based on lobate scarps imaged by both MESSENGER and Mariner 10 increase to 0.06% (Watters et al., 2009), corresponding to a 700 m decrease in radius (Watters et al., 2009; Watters and Nimmo, 2010).

Based on topographic analyses of contractional structures by stereo imaging (Strom et al., 1975; Watters, 1988) and Mercury Laser Altimeter (MLA), typical shortening accommodated per structure exceeds that of martian ridges (Zuber et al., 2010). However, these studies use the maximum displacement to determine the fault-related strain and corresponding radius decrease, which are too high by a factor of 2 (see Section 3.2.2 above for Mars). As noted above, previous strain and radius change calculations performed for Mercury using fault scaling use the maximum displacement and thereby over-predict the amount of contraction and radius decrease. Watters et al. (1998) and Watters and Nimmo (2010) also use D/L scaling and the large-fault approximation, where the downdip fault height H is equal to the depth of faulting T, to estimate horizontal contractional strain on Mercury accommodated by lobate scarps and wrinkle ridges. The large-fault solution used by Watters et al. (1998) to calculate contractional strain and planetary radius decrease for Mercury is comparable to, or perhaps half of, the actual value that is implied by a constant D/L ratio and the small-fault form of Kostrov's equation.

Estimates of the global contractional strain and radius change for Mercury are critical to providing constraints for thermal evolution models (Melosh and McKinnon, 1988; Watters et al., 2009; Watters and Nimmo, 2010; Zuber et al., 2010) and have been used for this purpose (Hauck et al., 2004; Watters et al., 2004). Existing thermal history models (e.g., Solomon, 1976, 1977; Schubert et al., 1988; Spohn, 1991; Solomatov and Reese, 2001; Hauck et al., 2004; Williams et al., 2007) predict radius decreases several times larger than can be accommodated by observed lobate scarps (Watters et al., 1998; Dombard et al., 2001; Watters et al., 2009; Watters and Nimmo, 2010), paralleling our results for Mars.

The discrepancy between the observed and predicted strains from these models has led to the suggestion that low-amplitude, long-wavelength (>100 km) folds may accommodate horizontal contraction of magnitude similar to what is recorded by the lobate scarps (Dombard et al., 2001; Watters et al., 2009; Watters and Nimmo, 2010). However, a recent study implies that the contractional deformation on Mercury has been primarily the result of movement along deeply penetrating faults that were active over a long portion of Mercury's history (Zuber et al., 2010), as suggested for martian wrinkle ridges on Solis Planum (Montési and Zuber, 2003). An alternative explanation is that, since the majority of observed lobate scarps appears to have formed after the emplacement of the youngest Calorian smooth plains (~3.2 Ga; Tanaka and Hartmann, 2008), they may only record part of the strain accumulated during planetary contraction (Watters and Nimmo, 2010).

4.3. Implications for planetary thermal model development

A common challenge for planetary thermal evolution models is the significant overprediction of global contraction that has been accommodated by the contractional structures at their surfaces (e.g., Mercury, the Moon, and Mars). Several possible explanations for these discrepancies suggested in the literature include long-wavelength, low-amplitude folds not visible in imagery or currently available topography (Dombard et al., 2001), near-surface regolith accommodating more contraction than intact rock before failing (Binder and Gunga, 1985; Pritchard and Stevenson, 2000; Watters and Nimmo, 2010), non-monotonic thermal histories (Pritchard and Stevenson, 2000), accommodation by many small faults (Weisberg and Hager, 1998; Pritchard and Stevenson, 2000; Watters and Nimmo, 2010), or that the crust can accommodate a small amount of elastic strain without brittle failure (Watters and Nimmo, 2010).

Estimates of total fault strain and moment release are dominated by the largest faults in an area, as implied by Eq. (3) (Scholz and Cowie, 1990; Scholz, 1997, 2002; Schultz, 2003). By implication, a hypothetical set of faults smaller than those observed and mapped on Mars by Knapmeyer et al. (2006, 2008) or on Mercury would contribute an insignificant amount to the contractional strain and radius decrease and would not account for the strain discrepancy between the thermal models and fault-related strain reported in this and other studies. Similarly, studies of fault-related strain (e.g., Scholz 1997, 2002, p. 307) and fault localization (Montési and Zuber, 2003) indicate that the magnitudes of strain accommodated by faults generally exceed those of unfaulted lithosphere, effectively prohibiting this notion from providing the large values of additional strain implied by the thermal history models. On Mars and likely Mercury, the volume of regolith is considerably smaller than that of faulted lithosphere, diminishing the potential contribution of regolith strain (even before it faults) to the global contractional strain.

Given the robustness of calculated strain and planetary radius changes associated with thrust and normal faults, we suggest that fault populations provide a tighter constraint on planetary thermal histories than do the thermal models alone. This comparison is well accepted for thermal models for the Moon, where the lack of a global distribution of faults has been used as reliable evidence that no significant radius change has occurred (Solomon and Chaiken, 1976; Cordell and Strom, 1977; Solomon, 1986; Solomon and Head, 1979, 1980; Golombek and McGill, 1983; Watters and Johnson, 2010; Watters et al., 2010), adding an important constraint for lunar thermal models. We suggest that using the observed geologic and tectonic records as a basis for calibration can refine thermal evolution models for Mars and potentially Mercury.

5. Conclusions

The hypothesis of a period of global contraction on Mars during the Late Noachian–Early Hesperian is quantitatively tested. We calculate fault-related contractional strains based on a recent fault compilation (Knapmeyer et al., 2006, 2008) and compare these

results to the contractional strains predicted by thermal models (Hauck and Phillips, 2002; Andrews-Hanna et al., 2008). The calculations were carried out for two time periods: the Late Noachian–Early Hesperian (LN–EH), the time of the hypothesized pulse of global contraction, and the Early Noachian–Late Amazonian (EN–LA), the time of preserved history on Mars, and a range of plausible fault scaling relationships. Contractional strain due to these structures for the Late Noachian–Early Hesperian pulse is calculated to be between −0.007% and −0.222%. Values of strain were converted to planetary radius decreases between 112 m and 3.77 km.

Incorporating extensional structures that also formed during these time periods provides values for the net planetary radius change, assuming that they also resulted from global-scale processes. The large values of globally averaged extensional strain accommodated by normal faults over martian history attest to the fundamental contribution of local and regional tectonics, such as Tharsis, to the planet's topography and structural development.

Contractional strain for the Hesperian pulse makes up ~59% of the total accumulated contractional strain for all of Mars' observable geologic history. Based on these results, our work is consistent with prior suggestions of a period of enhanced global contractional deformation that occurred between the Late Noachian and Early Hesperian, although the contribution of Tharsis-centered and impact basin-centered contractional deformation is likely to have been significant during this time interval. Previous work on a terrestrial analog to wrinkle ridges indicates that folding and thrust faulting that formed the Yakima folds in central Washington State may have occurred in response to subsidence of a basalt-filled basin (Reidel et al., 1989) with their orientations related to a regional stress state (Schultz and Watters, 1995) that was associated with oblique subduction (e.g., Reidel et al., 1984; Humphreys, 2009). We hypothesize that wrinkle ridges in Hesperian basalts on Mars may also reflect a component of local subsidence with ridge orientations related to the regional stress state (e.g., Tharsis).

The calculated fault-related strains were compared to predictions of contractional strain from thermal models. We find that thermal models generally over-predict the amount of strain that was accommodated at the surface by observed faults by 1.3–27.9 times and the amount of net planetary radius change by ~310 m to ~5 km, depending on the time period of interest. Comparable thermal history models for Mercury and the Moon also over-predict the amount of radius decrease and by similar amounts. We conclude that structures observed at the surface provide a useful constraint along with assumptions of planetary composition for the construction of planetary thermal evolution models, even for tectonically complex planets such as Mars. Tectonic strain rates can also be used as constraints for future thermal models.

Acknowledgments

This work was supported in part by a grant from NASA's Mars Data Analysis Program to RAS. The authors thank two anonymous reviewers for reviews that strengthened and clarified the final paper. We thank Jeff Andrews-Hanna for interesting and helpful discussions and for sharing his thermal strain calculations, Martin Knapmeyer at DLR for sharing the most recent Mars fault catalog, and Matt Weller at Rice University for help in producing Fig. 1. This is LPI Contribution 1566.

References

Andrews-Hanna, J.C., Zuber, M.T., Hauck II, S.A., 2008. Strike-slip faults on Mars: Observations and implications for global tectonics and geodynamics. J. Geophys. Res. 113. E08002. doi:10.1029/2007JE002980.

Banerdt, W.B., Golombek, M.P., Tanaka, K.L., 1992. Stress and tectonics on Mars. In: Kieffer, H.H., Jakosky, B.M., Snyder, C.M., Matthews, M.S. (Eds.), Mars. Univ. of Arizona Press, Tucson, pp. 249–297.

Bergen, K.J., Shaw, J.H., 2010. Displacement profiles and displacement–length scaling relationships of thrust faults constrained by seismic-reflection data. Geol. Soc. Am. Bull. 122 (7/8), 1209–1219. doi:10.1130/B26373.

Beuthe, M., 2010. East–west faults due to planetary contraction. Icarus 209, 795–817. doi:10.1016/j.icarus.2010.04.019.

Binder, A.B., 1982. Post-Imbrian global lunar tectonism: Evidence for an initially totally molten Moon. Earth Moon Planets 26, 117–133.

Binder, A.B., Gunga, H.-C., 1985. Young thrust-fault scarps in the highlands: Evidence for an initially totally molten Moon. Icarus 63, 421–441.

Cailleau, B., Walter, T.R., Janle, P., Hauber, E., 2003. Modeling volcanic deformation in a regional stress field: Implications for the formation of graben structures on Alba Patera, Mars. J. Geophys. Res. 108, 5141. doi:10.1029/2003JE002135.

Carr, M.H., 1974. Tectonism and volcanism of the Tharsis region of Mars. J. Geophys. Res. 79, 3943–3949.

Cassen, P., Reynolds, R.T., Peale, S.J., 1979. Is there liquid water on Europa? Geophys. Res. Lett. 6, 732–734.

Cohen, S.C., 1999. Numerical models of crustal deformation in seismic zones. Adv. Geophys. 41, 133–231.

Collins, G.C., McKinnon, W.B., Moore, J.M., Nimmo, F., Pappalardo, R.T., Prockter, L.M., Schenk, P.M., 2010. Tectonics of the outer planet satellites. In: Watters, T.R., Schultz, R.A. (Eds.), Planetary Tectonics. Cambridge Univ. Press, Cambridge, UK, pp. 264–350.

Cordell, B.M., Strom, R.G., 1977. Global tectonics of Mercury and the Moon. Phys. Earth Planet. Int. 15, 146–155.

Dawers, N.H., Anders, M.H., Scholz, C.H., 1993. Growth of normal faults: Displacement–length scaling. Geology 21, 1107–1110.

Dimitrova, L.L., Holts, W.E., Haines, A.J., Schultz, R.A., 2008. Stress models, global contraction, and surface faults on Mars. Lunar Planet. Sci. XXXIX. Abstract 1848.

Dombard, A.J., Hauck, S.A., Solomon, S.C., Phillips, R.J., 2001. Potential for long-wavelength folding on Mercury. Lunar Planet. Sci. XXXII. Abstract 2035.

Elkins-Tanton, L.T., Hess, P.C., Parmentier, E.M., 2005. Possible formation of ancient crust on Mars through magma ocean processes. J. Geophys. Res. 110. E12S01. doi:10.1029/2005JE002480.

Frey, H.V., 1992. Thermal history and climatic implications of early Hesperian ages for presumed Noachian age volcanic flows on Mars. Lunar Planet. Sci. XXIII, 385–386.

Golombek, M.P., McGill, G.E., 1983. Grabens, basin tectonics, and the maximum total expansion of the Moon. J. Geophys. Res. 88, 3563–3578.

Golombek, M.P., Phillips, R.J., 2010. Mars tectonics. In: Watters, T.R., Schultz, R.A. (Eds.), Planetary Tectonics. Cambridge Univ. Press, Cambridge, UK, pp. 183–232.

Greeley, R., Guest, J.E., 1987. Geologic Map of the Eastern Equatorial Region of Mars. 1:15,000,000 US Geological Survey Misc. Invest. Ser. I-1802-B.

Greeley, R., Schneid, B.D., 1991. Magma generation on Mars: Amounts, rates, and comparisons with Earth, Moon, and Venus. Science 254, 996–998.

Grott, M., Hauber, E., Werner, S.C., Kronberg, P., Neukum, G., 2007. Mechanical modeling of thrust faults in the Thaumasia region, Mars, and implications for the Noachian heat flux. Icarus 186, 517–526. doi:10.1016/j.icarus.2006.10.001.

Hartmann, W.K., 1973. Martian surface and crust: Review and synthesis. Icarus 19, 550–575.

Hartmann, W.K., Neukum, G., 2001. Cratering chronology and the evolution of Mars. Space Sci. Rev. 96, 165–194.

Hauber, E., Kronberg, P., 2001. Tempe Fossae, Mars: A planetary analogon to a terrestrial continental rift? J. Geophys. Res. 106, 165–194.

Hauber, E., Kronberg, P., 2005. The large Thaumasia graben on Mars: Is it a rift? J. Geophys. Res. 110. E07003. doi:10.1029/2005JE002407.

Hauber, E., Grott, M., Kronberg, P., 2010. Martian rifts: Structural geology and geophysics. Earth Planet. Sci. Lett. 294, 393–410. doi:10.1016/j.epsl.2009.11.005.

Hauck, S.A., Phillips, R.J., 2002. Thermal and crustal evolution of Mars. J. Geophys. Res. 107, 5052. doi:10.1029/2001JE001801.

Hauck II, S.A., Solomon, S.C., Phillips, R.J., 2003. Potential sources of Hesperian contractional tectonics on Mars. Lunar Planet. Sci. XXXIV. Abstract 1667.

Hauck II, S.A., Dombard, A.J., Phillips, R.J., Solomon, S.C., 2004. Internal and tectonic evolution of Mercury. Earth Planet. Sci. Lett. 222, 713–728.

Head III, J.W., Kreslavsky, M.A., Pratt, S., 2002. Northern lowlands of Mars: Evidence for widespread volcanic flooding and tectonic deformation in the Hesperian period. J. Geophys. Res. 107, 5003. doi:10.1029/2000JE001445.

Howard, K.A., Muehlberger, W.R., 1973. Lunar Thrust Faults in the Taurus-Littrow Region. Apollo 17 Preliminary Science Report, NASA Spec. Publ., SP-330, 31-22 to 31-25.

Humphreys, E., 2009. Relation of flat subduction to magmatism and deformation in the western United States. In: Kay, S.M., Ramos, V.A., Dickinson, W.R. (Eds.), Backbone of the Americas: Shallow Subduction, Plateau Uplift, and Ridge and Terrane Collision, vol. 204. Geol. Soc. Am. Mem., pp. 1–13.

Ivanov, M.A., Head, J.W., 2006. Alba Patera, Mars: Topography, structure, and evolution of a unique Late Hesperian–Early Amazonian shield volcano. J. Geophys. Res. 111. E09003. doi:10.1029/2005JE002469.

Knapmeyer, M., Oberst, J., Hauber, E., Wählisch, M., Deuchler, C., Wagner, R., 2006. Working models for spatial distribution and level of Mars' seismicity. J. Geophys. Res. 111. doi:10.1029/2006JE002708.

Knapmeyer, M., Schneider, S., Misun, M., Wählisch, M., Hauber, E., 2008. An extended global inventory of Mars Surface Faults [abs.], vol. 10, European Geophysical Union General Assembly: Vienna, Austria, European Geophysical Union.

Lee, D.-C., Halliday, A.N., 1997. Core formation on Mars and differentiated asteroids. Nature 338, 854–857.

Lodders, K., Fegley Jr., B., 1997. An oxygen isotope model for the composition of Mars. Icarus 126, 373–394.
Lucchitta, B.K., 1976. Mare ridges and related highland scarps—Results of vertical tectonism. Proc. Lunar Sci. Conf. 7th, Houston, Tex., vol. 3, March 15–19, pp. 2761–2782.
Mangold, N., Allemand, P., Thomas, P.G., Vidal, G., 2000. Chronology of compressional deformation on Mars: Evidence for a single and global origin. Planet. Space Sci. 48, 1201–1211.
Manighetti, I., Campillo, M., Sammis, C., Mai, P.M., King, G., 2005. Evidence for self-similar, triangular slip distributions on earthquakes: Implications for earthquake and fault mechanics. J. Geophys. Res. 110. B05302. doi:10.1029/2004JB003174.
Marone, C., 1998. Laboratory-derived friction laws and their application to seismic faulting. Annu. Rev. Earth Planet. Sci. 26, 643–696.
McGovern, P.J., Solomon, S.C., Faulkner, S.E., Head, J.W., Smith, D.E., Zuber, M.T., 1999. Extension and volcanic loading at Alba Patera: Insights from MOLA observations and loading models. Lunar Planet. Sci. XXX. Abstract 1697.
McGovern, P., Solomon, S., Head III, J., Smith, D., Zuber, M., Neumann, G., 2001. Extension and uplift at Alba Patera, Mars: Insights from MOLA observations and loading models. J. Geophys. Res. 106, 23769–23809.
Mège, D., Masson, P., 1996. A plume tectonics model for the Tharsis Province, Mars. Planet. Space Sci. 44, 749–782.
Melosh, H.J., McKinnon, W.B., 1988. The tectonics of Mercury. In: Vilas, F., Chapman, C.R., Matthews, M.S. (Eds.), Mercury. Univ. of Arizona Press, Tuscon, pp. 374–400.
Montési, L.G.J., Zuber, M.T., 2003. Clues to the lithospheric structure of Mars from wrinkle ridge sets and localization instability. J. Geophys. Res. 108, 5048. doi:10.1029/2002JE001974.
Mueller, S., McKinnon, W.B., 1988. Three-layered models for Ganymede and Callisto: Compositions, structures, and aspects of evolution. Icarus 76, 437–464.
Murray, B.C., Belton, M.J.S., Danielson, G.E., Davies, M.E., Gault, D.E., Hapke, B., O'Leary, B., Strom, R.G., Suomi, V., Trask, N., 1974. Mercury's surface: Preliminary description and interpretation from Mariner 10 pictures. Science 185, 169–179.
Nimmo, F., 2004. Stresses generated in cooling viscoelastic ice shells: Application to Europa. J. Geophys Res. 109. E12001. doi:10.1029/2003JE002168.
Okubo, C.H., Schultz, R.A., 2004. Mechanical stratigraphy in the western equatorial region of Mars based on thrust fault-related fold topography and implications for near-surface volatile reservoirs. Geol. Soc. Am. Bull. 116, 594–605. doi:10.1130/B25361.1.
Plescia, J.B., Golombek, M.P., 1986. Origin of planetary wrinkle ridges based on the study of terrestrial analogs. Geol. Soc. Am. Bull. 97, 1289–1299.
Polit, A.T., Schultz, R.A., Soliva, R., 2009. Geometry, displacement–length scaling, and extensional strain of normal faults on Mars with inferences on mechanical stratigraphy of the martian crust. J. Struct. Geol. 31, 662–673. doi:10.1016/j.jsg.2009.03.016.
Pritchard, M.E., Stevenson, D.J., 2000. Thermal aspects of a lunar origin by giant impact. In: Canup, R., Righter, K. (Eds.), Origin of the Earth and Moon. Univ. of Arizona Press, Tucson, pp. 179–196.
Reidel, S.P., Scott, G.R., Bazard, D.R., Cross, R.W., Dick, B., 1984. Post-12 million year clockwise rotation in the Central Columbia Plateau, Washington. Tectonics 3, 251–273. doi:10.1029/TC003i002p00251.
Reidel, S.P., Fecht, K.R., Hagood, M.C., Tolan, T.L., 1989. The geologic evolution of the central Columbia Plateau. In: Reidel, S.P., Hooper, P.R. (Eds.), Volcanism and Tectonism in the Columbia River Flood-basalt Province. Geol. Soc. Am. Spec. Paper, vol. 239, pp. 247–264.
Scholz, C.H., 1982. Scaling laws for large earthquakes: Consequences for physical models. Bull. Seis. Soc. Am. 72, 1–14.
Scholz, C.H., 1997. Earthquake and fault populations and the calculation of brittle strain. Geowissenschaften 15, 124–130.
Scholz, C.H., 1998. Earthquakes and friction laws. Nature 391, 37–42.
Scholz, C.H., 2002. The Mechanics of Earthquakes and Faulting, second ed. Cambridge University Press, Cambridge, UK.
Scholz, C.H., Cowie, P.A., 1990. Determination of total strain from faulting using slip measurements. Nature 346, 837–838.
Schubert, G., Spohn, T., 1990. Thermal history of Mars and the sulfur content of its core. J. Geophys. Res. 95, 14095–14104.
Schubert, G., Ross, M.N., Stevenson, M.J., Spohn, T., 1988. Mercury's thermal history and the generation of its magnetic field. In: Vilas, F., Chapman, C.R., Matthews, M.S. (Eds.), Mercury. Univ. of Arizona Press, Tucson, pp. 429–460.
Schubert, G., Solomon, S.C., Turcotte, D.L., Drake, M.J., Sleep, N.H., 1992. Origin and thermal evolution of Mars. In: Kieffer, H.H., Jakosky, B.M., Snyder, C.M., Matthews, M.S. (Eds.), Mars. Univ. of Arizona Press, Tuscon, pp. 147–183.
Schultz, R.A., 2000. Localization of bedding plane slip and backthrust faults above blind thrust faults: Keys to wrinkle ridge structure. J. Geophys. Res. 105, 12035–12052.
Schultz, R.A., 2003. Seismotectonics of the Amenthes Rupes thrust fault population, Mars. Geophys. Res. Lett. 30, 1303. doi:10.1029/2002GL016475.
Schultz, R.A., Watters, T.R., 1995. Elastic buckling of fractured basalt on the Columbia Plateau, Washington State. In: Daemen, J.J.K., Schultz, R.A. (Eds.), Rock Mechanics: Proceedings of the 35th US Symposium, Balkema, Rotterdam, pp. 855–860.
Schultz, R.A., Watters, T.R., 2001. Forward mechanical modeling of the Amenthes Rupes thrust fault on Mars. Geophys. Res. Lett. 28, 4659–4662.
Schultz, R.A., Okubo, C.H., Wilkins, S.J., 2006. Displacement–length scaling relations for faults on the terrestrial planets. J. Struct. Geol. 28, 2182–2193. doi:10.1016/j.jsg.2006.03.034.
Schultz, R.A., Soliva, R., Okubo, C.H., Mège, D., 2010. Fault populations. In: Watters, T.R., Schultz, R.A. (Eds.), Planetary Tectonics. Cambridge University Press, Cambridge, UK, pp. 457–510.
Scott, D.H., Tanaka, K.L., 1986. Geologic Map of the Western Equatorial Region of Mars. 1:15,000,000. US Geological Survey Misc. Invest. Ser. I-1802-A.
Scott, D.H., Tanaka, K.L., Greeley, R., Guest, J.E., 1987a. Geologic Map of the Eastern Equatorial Region of Mars. 1:15,000,000. US Geological Survey Misc. Invest. Ser. I-1802-B.
Scott, D.H., Tanaka, K.L., Greeley, R., Guest, J.E., 1987b. Geologic Map of the Polar Regions of Mars. 1:15,000,000. US Geological Survey Misc. Invest. Ser. I-1802-C.
Scott, E.D., Wilson, L., Head III, J.W., 2002. Emplacement of giant radial dikes in the northern Tharsis region of Mars. J. Geophys. Res. 107, 5019. doi:10.1029/2000JE001431.
Searls, M.L., Phillips, R.J., 2007. Tectonics of Utopia Basin, Mars: Results from finite element loading models. Lunar Planet. Sci. XXXVIII. Abstract 1965.
Soliva, R., Schultz, R.A., Benedicto, A., 2005. Three-dimensional displacement–length scaling and maximum dimension of normal faults in layered rocks. Geophys. Res. Lett. 32. L16302. doi:10.1029/2005GL023007.
Solomatov, V.S., Reese, C.C., 2001. Mantle convection and thermal evolution of Mercury revisited. Workshop on Mercury: Space Environment, Surface, and Interior, vol. 1097. Lunar and Planetary Institute, Houston, pp. 92–95.
Solomon, S.C., 1976. Some aspects of core formation in Mercury. Icarus 28, 509–521.
Solomon, S.C., 1977. The relationship between crustal tectonics and internal evolution in the Moon and Mercury. Phys. Earth Planet. Int. 15, 135–145.
Solomon, S.C., 1986. On the Early Thermal State of the Moon. Lunar and Planetary Institute, Houston, TX. pp. 435–452.
Solomon, S.C., Chaiken, J., 1976. Thermal expansion and thermal stress in the Moon and terrestrial planets: Clues to early thermal history. Proc. Lunar Sci. Conf. 7th, 3229–3243.
Solomon, S.C., Head, J.W., 1979. Vertical movement in mare basins: Relation to mare emplacement, basin tectonics, and lunar thermal history. J. Geophys. Res. 84, 1667–1682.
Solomon, S.C., Head, J.W., 1980. Lunar mascon basins: Lava filling, tectonics, and evolution of the lithosphere. Rev. Geophys. Space Phys. 18, 107–141.
Spohn, T., 1991. Mantle differentiation and thermal evolution of Mars, Mercury, and Venus. Icarus 90, 222–236.
Squyres, S.W., 1980. Volume changes in Ganymede and Callisto and the origin of grooved terrain. Geophys. Res. Lett. 7, 593–596.
Squyres, S.W., Croft, S.K., 1986. The tectonics of icy satellites. In: Burns, J.A., Matthews, M.S. (Eds.), Satellites. Univ. of Arizona Press, Tucson, pp. 293–341.
Strom, R.G., Trask, N.J., Guest, J.E., 1975. Tectonism and volcanism on Mercury. J. Geophys. Res. 80, 2478–2507.
Tanaka, K.L., Hartmann, W.K., 2008. The planetary timescale. In: Ogg, J.G., Ogg, G.M., Gradstein, F.M. (Eds.), The Concise Geologic Time Scale. Cambridge Univ. Press, New York, pp. 13–22.
Tanaka, K.L., Isbell, N.K., Scott, D.H., Greeley, R., Guest, J.E., 1988. The resurfacing history of Mars: A synthesis of digitized, Viking-based geology. Proc. Lunar Sci. Conf. 18, 665–678.
Tanaka, K.L., Golombek, M.P., Banerdt, W.B., 1991. Reconciliation of stress and structural histories of the Tharsis region of Mars. J. Geophys. Res. 96, 15617–15633.
Tanaka, K.L., Anderson, R., Dohm, J.M., Hansen, V.L., McGill, G.E., Pappalardo, R.T., Schultz, R.A., Watters, T.R., 2010. Planetary structural mapping. In: Watters, T.R., Schultz, R.A. (Eds.), Planetary Tectonics. Cambridge Univ. Press, Cambridge, UK, pp. 351–396.
Thomas, P.G., Masson, P., Fleitout, L., 1988. Tectonic history of Mercury. In: Vilas, F., Chapman, C.R., Matthews, M.S. (Eds.), Mercury. Univ. of Arizona Press, Tucson, pp. 401–428.
Trask, N.J., Guest, J.E., 1975. Preliminary geologic terrain map of Mercury. J. Geophys. Res. 80, 2461–2477.
Tse, S., Rice, J., 1986. Crustal earthquake instability in relation to the depth variation of frictional slip properties. J. Geophys. Res. 91, 9452–9472.
Turcotte, D.L., 1983. Thermal stresses in planetary elastic lithospheres. Proc. 13th Lunar Planet. Sci., J. Geophys. Res. 88, A585–A587.
Wänke, H., Dreibus, G., 1994. Chemistry and accretion history of Mars. Philos. Trans. R. Soc. Lond. 349, 285–293.
Watters, T.R., 1988. Wrinkle ridge assemblages on the terrestrial planets. J. Geophys. Res. 93, 10236–10254.
Watters, T.R., 1993. Compressional tectonism on Mars. J. Geophys. Res. 98, 17049–17060.
Watters, T.R., 2003a. Lithospheric flexure and the origin of the dichotomy boundary on Mars. Geology 31, 271–274.
Watters, T.R., 2003b. Thrust faulting along the dichotomy boundary in the eastern hemisphere of Mars. J. Geophys. Res. 108, 5055. doi:10.1029/2002JE001934.
Watters, T.R., Johnson, C.L., 2010. Lunar tectonics. In: Watters, T.R., Schultz, R.A. (Eds.), Planetary Tectonics. Cambridge Univ. Press, Cambridge, UK, pp. 121–182.
Watters, T.R., Maxwell, T.A., 1983. Crosscutting relations and relative ages of ridges and faults in the Tharsis region of Mars. Icarus 56, 278–298.
Watters, T.R., Maxwell, T.A., 1986. Orientation, relative age, and extent of the Tharsis Plateau ridge system. J. Geophys. Res. 91, 8113–8125.
Watters, T.R., Nimmo, F., 2010. The tectonics of Mercury. In: Watters, T.R., Schultz, R.A. (Eds.), Planetary Tectonics. Cambridge Univ. Press, Cambridge, UK, pp. 15–79.
Watters, T.R., Robinson, M.S., Cook, A.C., 1998. Topography of lobate scarps on Mercury: New constraints on the planet's contraction. Geology 26, 991–994.

Watters, T.R., Robinson, M.S., Bina, C.R., Spudis, P.D., 2004. Thrust faults and the global contraction of Mercury. Geophys. Res. Lett. 31. L04701. doi:10.1029/2003GL019171.

Watters, T.R., Solomon, S.C., Robinson, M.S., Head, J.W., André, S.L., Hauck II, S.A., Murchie, S.L., 2009. The tectonics of Mercury: The view after MESSENGER's first flyby. Earth Planet. Sci. Lett. 285, 283–296. doi:10.1016/j.epsl.2009.01.025.

Watters, T.R. et al., 2010. Evidence of recent thrust faulting on the Moon revealed by the Lunar Reconnaissance Orbiter Camera. Science 329, 936–940. doi:10.1126/science.1189590.

Weisberg, O., Hager, B.H., 1998. Global lunar contraction with subdued surface topography. In: Origin of the Earth and Moon, December 1–3, 1998. Lunar and Planetary Institute, Houston, Monterey, CA, p. 54.

Wilkins, S.J., Schultz, R.A., 2005. 3D cohesive end-zone model for source scaling of strike-slip interplate earthquakes. Bull. Seis. Soc. Am. 95, 2232–2258.

Wilkins, S.J., Schultz, R.A., Anderson, R.C., Dohm, J.M., Dawers, N.H., 2002. Deformation rates from faulting at the Tempe Terra extensional province, Mars. Geophys. Res. Lett. 29, 1884. doi:10.1029/2002GL015391.

Williams, J.-P., Aharonson, O., Nimmo, F., 2007. Powering Mercury's dynamo. Geophys. Res. Lett. 34. L21201. doi:10.1029/2007GL031164.

Wilson, L., Head III, J.W., 2002. Tharsis-radial graben systems as the surface manifestation of plume-related dike intrusion complexes: Models and implications. J. Geophys. Res. 107, 5057. doi:10.1029/2001JE001593.

Wise, D.U., Golombek, M.P., McGill, G.E., 1979. Tharsis province of Mars: Geologic sequence, geometry, and a deformation mechanism. Icarus 38, 456–472.

Zimbelman, J.R., Solomon, S.C., Sharpton, V.L., 1991. The evolution of volcanism, tectonics, and volatiles on Mars: An overview of recent progress. Proc. Lunar Sci. 21, 613–626.

Zuber, M.T. et al., 2000. Internal structure and early thermal evolution of Mars from Mars Global Surveyor topography and gravity. Science 287 (5489), 1788–1793. doi:10.1126/science.287.5459.1788.

Zuber, M.T. et al., 2010. Accommodation of lithospheric shortening on Mercury from altimetric profiles of ridges and lobate scarps measured during MESSENGER flybys 1 and 2. Icarus 209, 247–255. doi:10.1016/j.icarus.2010.02.026.